Journal of Alloys and Compounds 515 (2012) 108–113

Contents lists available at SciVerse ScienceDirect

Journal of Alloys and Compounds

journal homepage: www.elsevier.com/locate/jallcom

Influence of Si and Fe on the distribution of intermetallic compounds in twin-roll cast Al–Mn–Zr alloys

M. Karlík*, T. Mánik, H. Lauschmann

Czech Technical University in Prague, Faculty of Nuclear Sciences and Physical Engineering, Department of Materials, Trojanova 13, 120 00 Praha 2, Czech Republic

ARTICLE INFO

Article history:
Received 16 September 2011
Received in revised form
18 November 2011
Accepted 22 November 2011
Available online 30 November 2011

Keywords:
Metals and alloys
Solid state reactions
Microstructure
Metallography
Scanning electron microscopy
Transmission electron microscopy

ABSTRACT

The aim of the experiments was to study the influence of Si and Fe on size and formation of secondary phases and recrystallization behavior of Al–Mn–Zr alloys prepared by twin-roll casting (TRC) in the industrial conditions. Microstructure (grain structure, phase composition, particle analysis) of these alloys was characterized during downstream processing. Quantitative particle analysis was carried out on FEG–SEM micrographs at both high and low magnifications. The phases were examined by light metallography, energy dispersive X-ray spectroscopy (EDXS) and by means of electron back-scattering diffraction (EBSD) according to their crystallographic structure. The microstructure at the final gauge was also observed by transmission electron microscope (TEM). A relatively high (0.5 wt.%) Si content and low (0.2 wt.%) Fe content in one of the alloys resulted in balancing of nucleation and dissolution rate for small particles. Hence a higher density of small particles was stable during the downstream processing, and this alloy showed improved recrystallization resistance.

1. Introduction

Al–Mn alloys, having good formability, thermal conductivity, and corrosion resistance, are commonly used for the production of the fins of automotive heat exchangers. The demands of further weight reduction and efficiency improvements imply thickness reduction of the fins below 0.1 mm. Even at the thickness of 0.05 mm, the mechanical strength of the fin should be sufficiently high to avoid buckling [1], and at the same time the alloy has to be recrystallization resistant to keep its strength after brazing at about 600 °C. In order to obtain such mechanical and technological properties, the alloy should contain a dense and homogeneous distribution of second phase particles to strengthen the alloy and also to exert a drag force (Zener drag) on moving subgrain and grain boundaries [2].

The best way to achieve a dense and homogeneous dispersion of second phase particles in Al alloys is to add a small amount (0.2–0.3 wt.%) of Sc leading to the formation of Al_3Sc dispersoids [3]. Unfortunately, scandium is extremely expensive and its commercial use is thus very limited. A similar effect can be obtained by Zr addition (0.2–0.8 wt.%), resulting in the formation of the Al_3Zr phase [4–6], having either metastable ($L1_2$) or stable ($D0_{23}$) crystal structure, depending on the thermal history of the alloy (heating/cooling rate during casting, homogenization procedure, etc.) [7–9].

All commercial aluminium alloys contain different amounts of silicon and iron as impurities or alloying additions, and these elements can in some cases deteriorate or improve their properties. Maximum values in Al–Mn alloys (AA3003) are: 0.6 wt.%Si, 0.7 wt.%Fe [10]. In the pure Al–Mn binary alloys, the decomposition of the supersaturated solid solution is very sluggish [11,12]. Additions of Fe and Si greatly decrease the solubility of Mn and accelerate the precipitation rate of secondary Mn-bearing phases, $Al_6(Fe,Mn)$ or α-$Al_{12}(Mn,Fe)_3Si$ [11–14]. Moreover, in Zr-containing alloys Fe and Si increase the rate of formation of Al_3Zr particles, acting as catalysts. The Al_3Zr dispersoids precipitate usually on the Si and Fe atom clusters [4]. Furthermore, Si has also a positive effect on Al_3Zr stability. The $D0_{22}$ compound $(Al_{0.72}Si_{0.28})_3Zr$ with Si atoms in its Al sublattice is more stable than $D0_{23}$ or $L1_2$ crystal structures [15]. One of the main problems of using Al_3Zr in order to inhibit recrystallization is that these dispersoids are usually heterogeneously distributed, due to the microsegregation of Zr and its low diffusivity [6]. A somewhat more homogeneous distribution of Al_3Zr particles can be achieved by a two-step precipitation annealing [5,16].

The size and distribution of intermetallic particles have a fundamental role not only in the recrystallization kinetics of the alloy, but also in controlling its microstructure evolution during downstream

* Corresponding author. Tel.: +420 224 358 507; fax: +420 224 358 523.
E-mail addresses: Miroslav.Karlik@fjfi.cvut.cz, karlik@kmat.fjfi.cvut.cz (M. Karlík).

0925-8388/$ – see front matter © 2011 Elsevier B.V. All rights reserved.
doi:10.1016/j.jallcom.2011.11.101

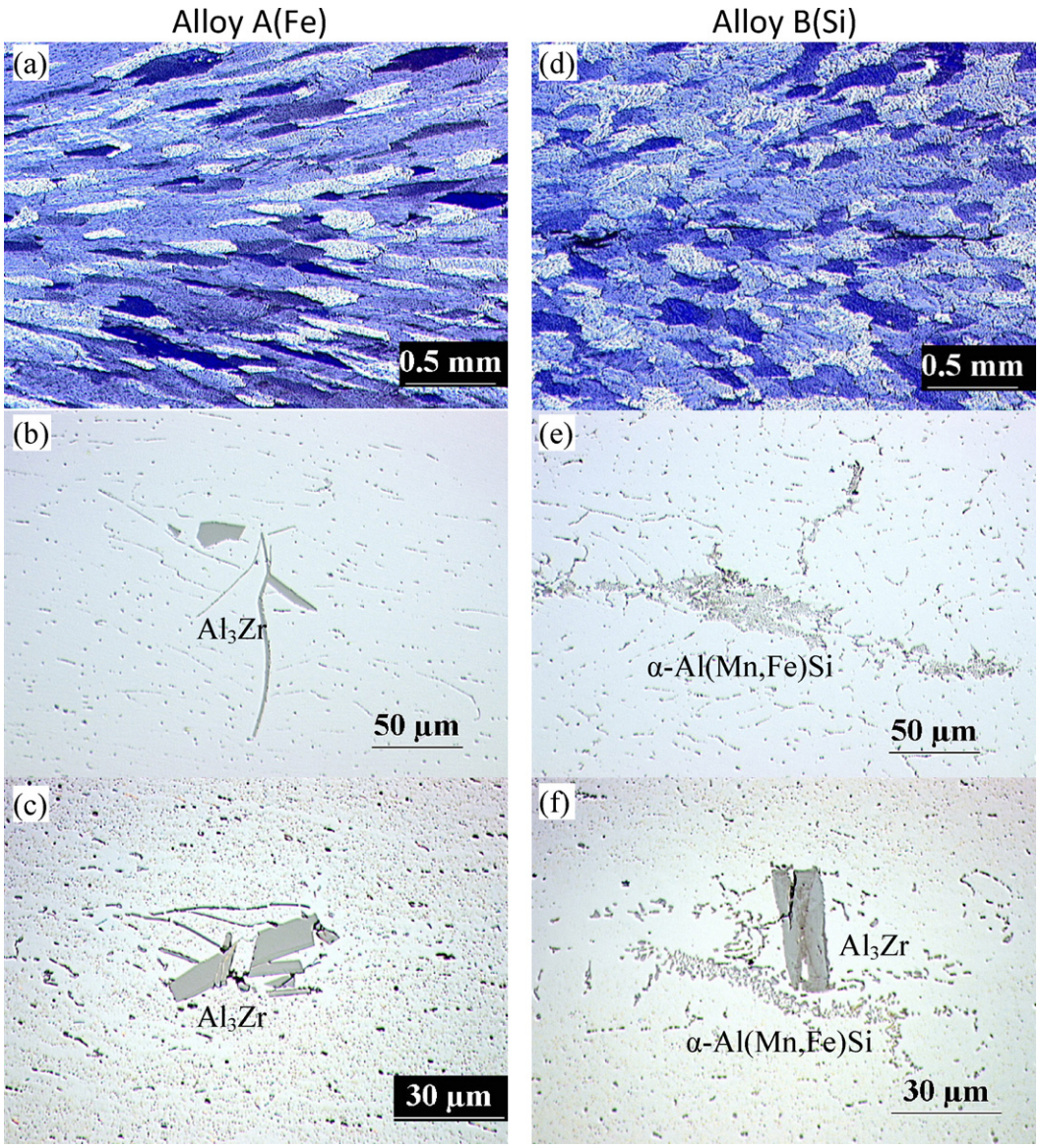

Fig. 1. Light micrographs of alloys at cast (8.5 mm) and 5.2 mm thicknesses: (a and d) Cast microstructure – grains; (b and e) cast microstructure – particles; (c and f) particles after precipitation annealing at 5.2 mm thickness.

processing. In addition to fine Al_3Zr dispersoids and large primary constituent phases, formed during solidification, Al–Mn alloys contain medium sized variously shaped Mn-containing dispersoids formed during heat treatment. These second phase particles ($Al_6(Fe,Mn)$ or α-$Al_{12}(Mn,Fe)_3Si$) can either stimulate or impede grain growth during thermomechanical treatment. Coarse particles (>1.5 μm) stimulate recrystallization by particle stimulated nucleation (PSN) mechanism, smaller particles (<0.5 μm) support Al_3Zr precipitate in exerting a dragging force on subgrain and grain boundaries [2].

The aim of the paper is to examine the influence of Si and Fe on the secondary phase particle distribution and recrystallization response of industrially twin-roll cast Al–Mn alloys with Zr addition.

2. Experimental details

The present investigation was carried out with two Al–Mn–Zr alloys. The alloy A contained higher amount of iron (0.32 wt.%) while the alloy B had higher amount of silicon (0.49 wt%), so they were denoted A(Fe) and B(Si), respectively. The content of other elements was very similar (Table 1). Industrially twin-roll cast strips, 8.5 mm in thickness, were processed in laboratory conditions. After cold rolling to 5.2 mm thickness (reduction 39%, equivalent strain $\varepsilon \sim 0.56$), the samples were subjected to a two-step precipitation annealing procedure involving 8 h heating to 250 °C, holding for 10 h at this temperature followed by 8 h heating to 450 °C, soaking for 12 h, and slow cooling (50 °C h^{-1}) [17]. Annealed samples were cold rolled to 0.3 mm thickness (reduction 94%, equivalent strain $\varepsilon \sim 3.3$) then recrystallization annealed for 3 h at 550 °C, and cold rolled to the final gauge of 0.065 mm (reduction 78%, equivalent strain $\varepsilon \sim 1.76$). Coarser particles in the precipitation annealed samples were analyzed by energy dispersive X-ray spectroscopy (EDXS) in the scanning electron microscope (SEM) FEI Quanta 200F equipped with a Schottky type field-emission gun (FEG) operated at 20 kV and also by electron back-scattering diffraction (EBSD) phase analysis according to their crystallographic structure.

The sheet samples were prepared with standard metallographic techniques: ground with SiC paper, polished with 3 μm diamond paste and finished with

Table 1
Chemical composition of studied alloys (wt.%).

Alloy	Mn	Zr	Fe	Si	Cu	Zn	Al
A(Fe)	1.10	0.17	0.32	0.13	0.15	0.10	Balance
B(Si)	1.06	0.17	0.18	0.49	0.13	0.10	Balance

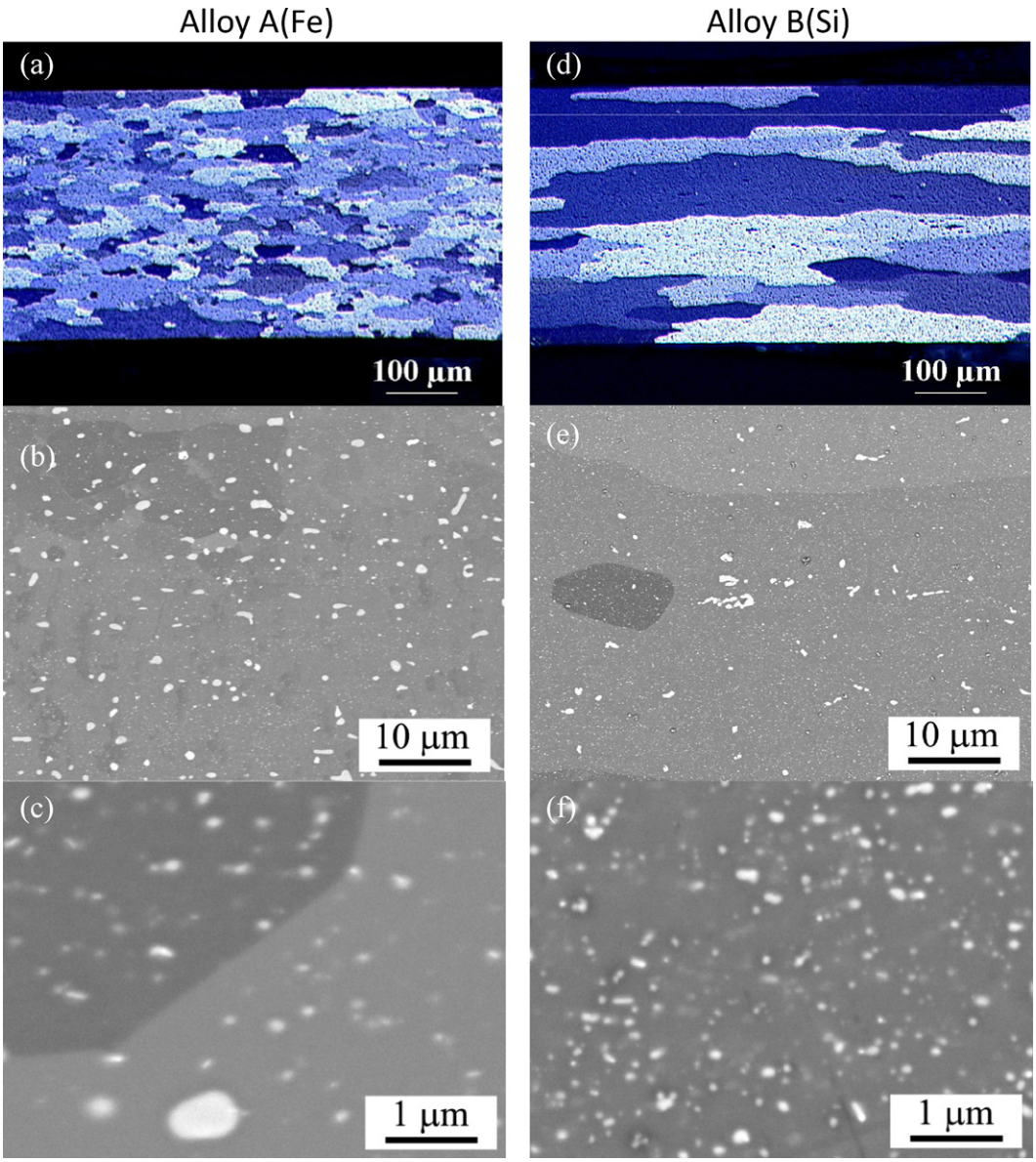

Fig. 2. Microstructure at 0.3 mm thickness: (a and d) Light micrographs of grains. (b and e) FEG SEM micrographs of coarse particles. (c and f) FEG SEM micrographs of fine particles.

colloidal silica. Their microstructure was studied using a Nikon Epiphot 300 metallographic microscope equipped with the camera Hitachi-HBC 20A. The second phase particles were revealed by etching with a 0.5% solution of hydrofluoric acid in water. The grain structure was visualized in polarized light after anodizing with Barker's reagent. Besides this basic microstructure examination, a quantitative second phase particle analysis on the series of FEG–SEM micrographs was carried out. The microscope was operated at 5 kV in the backscattered electron (BSE) signal. From each sample, 20 micrographs at the magnification 5000×, and 20 micrographs at the magnification 50 000× were recorded to examine coarse and fine second phase particles, respectively. This number of micrographs enabled to analyze more than 3000 particles to have a statistically sufficient data set [18]. The sets of micrographs were first normalized to have a constant mean value and standard deviation of brightness and then processed by the software written in Matlab [19], using toolboxes Image Processing and Statistics.

Samples at the final gauge 0.065 mm were subjected to isochronal annealing for 6 h in the temperature range from 260 to 400 °C. The recrystallization response was monitored on the 0.2% proof stress values obtained in tensile test. The microstructure of selected samples was also examined by means of EBSD and transmission electron microscopy (TEM). Standard 3 mm TEM discs were punched from the sheets and then twin-jet electropolished (at −20 °C, 15 V) using Struers Tenupol 2 apparatus filled with solution of 33% HNO_3 in methanol. The observations were carried out at 120 kV with JEOL JEM 1200EX microscope equipped with a CCD camera MegaView III.

3. Results

3.1. Microstructure at cast and 5.2 mm thickness

As it can be seen from Fig. 1a and d, both alloys show a similar grain structure, typical for twin-roll casting. The grains, 200–500 μm long, are oriented diagonally from the rolls to the center of the strip. They are somewhat more flattened in the case of alloy A(Fe) (Fig. 1a). Fig. 1b and e shows an illustration of coarse primary particles. Besides large blocks (>30 μm, Fig. 1c and f) or needles (>100 μm long, Fig. 1b) of the Al_3Zr phase, EDXS and EBSD analyses revealed cubic α-$Al_{12}(Mn,Fe)_2Si$ and orthorombic $Al_6(Mn,Fe)$ phase in the alloy A(Fe), while in the alloy B(Si) there was a mixture of cubic α-$Al_{12}(Mn,Fe)_2Si$ and hexagonal α-$Al_{15}(Mn,Fe)_3Si_2$ phases present also in the centerline segregation (Fig. 1e). Two-step precipitation annealing at the thickness of 5.2 mm increased the density of intermetallic particles, big blocks of primary Al_3Zr phase being still present in both alloys (Fig. 1c and f). However, the size and density of coarse particles of $Al_6(Mn,Fe)$

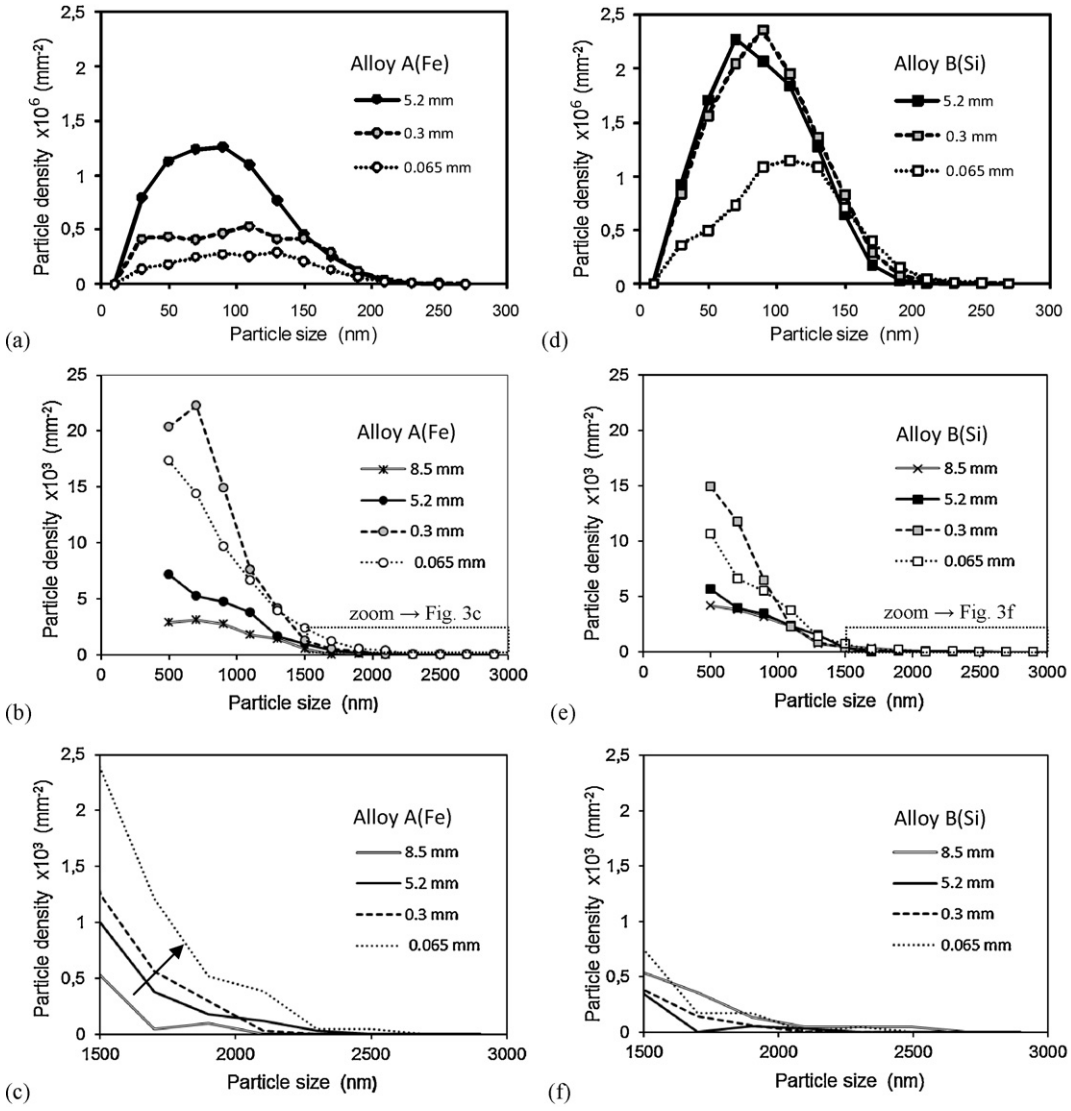

Fig. 3. Evolution of the distribution of particles in annealed sheets during downstream processing: (a and d) size 30 to 300 nm, (b and e) size 500–3000 nm (thickness 8.5 mm as cast, 5.2 mm – two step precipitation annealing 250/450 °C, 0.3 mm – intermediate annealing 550 °C/3 h, 0.065 mm – final annealing 320 °C/6 h), (c and f) particles greater than 1.5 μm (zoom of b and e, the arrow in c points out a significant increase of density of coarse particles in the alloy A(Fe)).

and cubic α-$Al_{12}(Mn,Fe)_2Si$ phases in alloy A(Fe) was clearly higher (Fig. 1c) than corresponding particles (except centerline segregation) in alloy B(Si) (Fig. 1f). This observation was also confirmed by quantitative particle analysis on a representative set of FEG SEM micrographs (Fig. 3b and e).

3.2. Microstructure at 0.3 mm thickness

A comparison of the microstructure of the alloys at 0.3 mm thickness after intermediate heat treatment for 3 h at 550 °C is in Fig. 2. Both alloys are fully recrystallized, but their grain structure and particle dispersion are distinctly different. The alloy A(Fe) shows very fine grains, 50–100 μm long in the center of the strip, and up to 200–300 μm on its surface, while the grains in the alloy B(Si) are very coarse, several hundreds of micrometres long. This difference is due to particle stimulated nucleation in alloy A(Fe), containing a dense distribution of coarse particles, as it can be noticed on light micrographs at 5.2 mm thickness (Fig. 1c), on FEG SEM micrographs at 0.3 mm thickness (Fig. 2b), as well as on the results of their analysis (Fig. 3b, c, e, and f). On the other hand, the alloy B(Si) contains much lower density of coarse particles which could provoke particle stimulated nucleation. This can be seen in Fig. 1f, and in Fig. 2e for 5.2 mm, and 0.3 mm thicknesses, respectively, and also from the graphs in Fig. 3c and f. As for fine particles (30–200 nm), important for blocking of the movement of subgrain and grain boundaries (Zener drag), the situation is opposite – their density in the alloy A(Fe) is much lower (Figs. 2c and 3a) than in the alloy B(Si) (Figs. 2f and 3d).

3.3. Microstructure at the final gauge

Light micrographs of the sheets at the final gauge 0.065 mm are in Fig. 4. Both alloys show a fibrous grain structure, which is somewhat more uniform in the alloy B(Si) (Fig. 4c), due to much higher initial grain size (Fig. 2d). There is again a distinct difference in the size and distribution of intermetallic particles – they are coarser in the alloy A(Fe) (Figs. 4b and 3b, c, e, f) and more densely distributed in alloy B(Si) (Figs. 4d and 3a, d). The resistance of such microstructures to recrystallization was checked on the evolution of 0.2% proof stress after isochronal annealing for 6 h in the temperature range 260–400 °C (Fig. 5). From the sharp decrease in the plots it can be seen that recrystallization of the alloy A(Fe) at these conditions

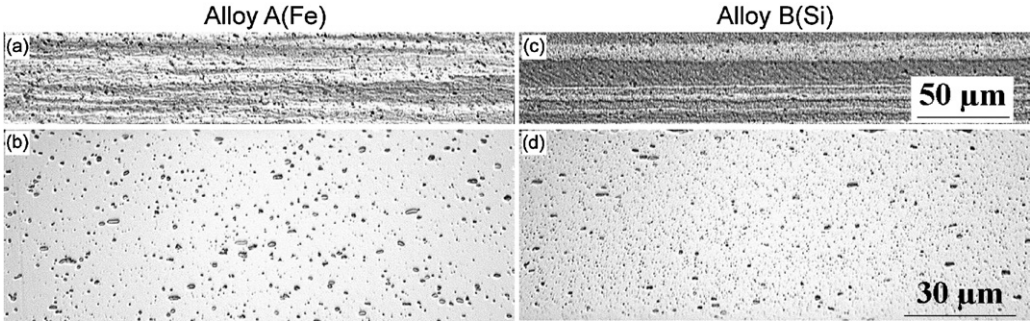

Fig. 4. Light micrographs of alloys at 0.065 mm thickness: (a and c) fibrous grains after cold rolling, (b and d) coarse particles.

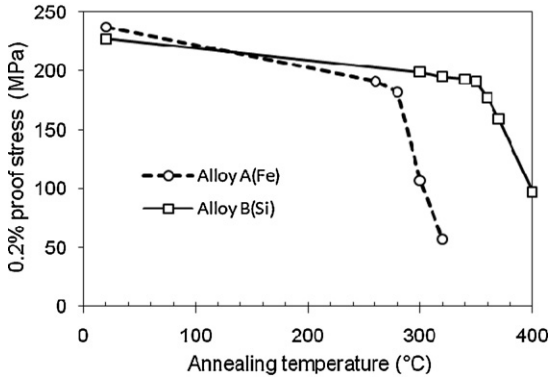

Fig. 5. Evolution of 0.2% proof stress of the foils at the final gauge 0.065 mm after annealing for 6 h at given temperature.

starts at temperatures over 280 °C, while the onset of recrystallization for the alloy B(Si) is shifted to temperatures beyond 350 °C. EBSD scans and TEM micrographs of the alloys annealed for 6 h at 320 °C are in Fig. 6. It is evident that alloy A(Fe) is almost fully recrystallized, showing large grains with only residual substructure (Fig. 6a and b), while alloy B(Si) is only recovered, containing many subgrains about 1 µm in size (Fig. 6b and c), effectively blocked in their growth by a fine dispersion of second phase particles.

4. Discussion

The difference in the iron and silicon content (alloy A(Fe) 0.32 wt.%Fe, 0.13 wt.%Si; alloy B(Si) 0.18 wt.%Fe, 0.49 wt.%Si) had only a negligible influence on the grain size and morphology of the strips at the cast and 5.2 mm thicknesses. The coarse particle distribution at the cast thickness of 8.5 mm was also nearly the same (Fig. 3c and f) (fine particles were scarcely formed in the as cast condition and so they were not quantified). However, an important difference was in the composition of constituent

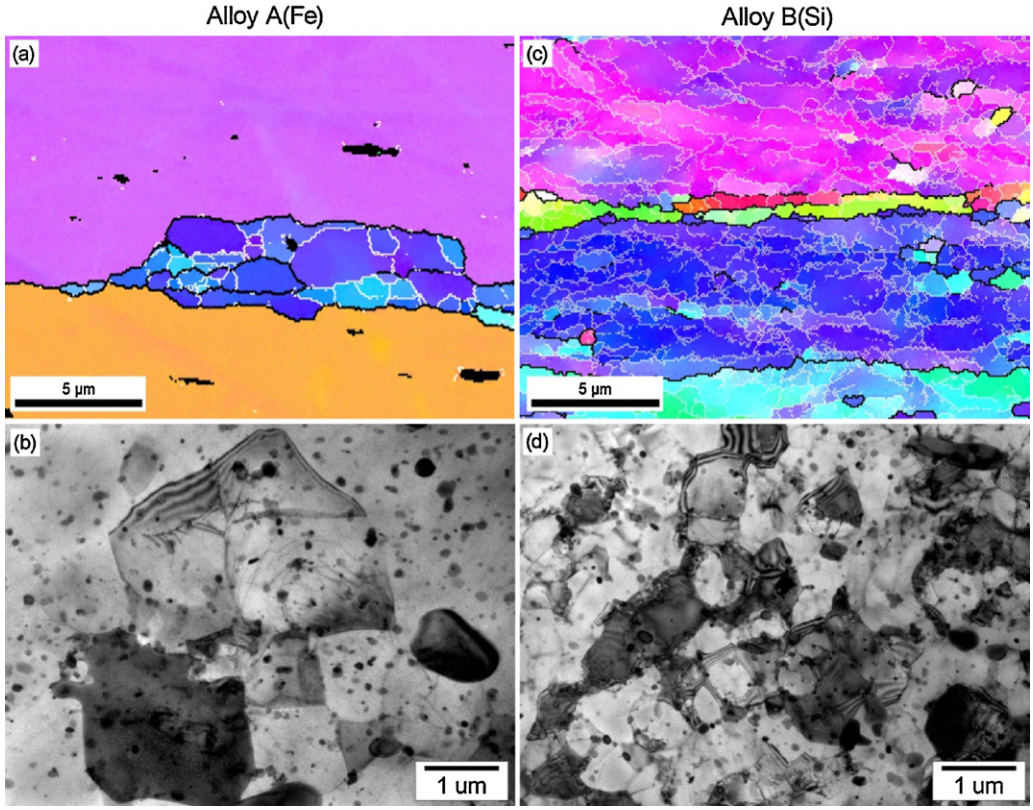

Fig. 6. Final microstructure of the alloys after cold rolling to 0.065 mm followed by annealing 320 °C/6 h: (a and c) EBSD orientation maps (high-angle boundaries are depicted by black lines and low-angle boundaries by white lines), (b and d) corresponding TEM micrographs.

phases. The alloy A(Fe) with the excess of Fe over Si contained orthorombic $Al_6(Mn,Fe)$ and cubic α-$Al_{12}(Mn,Fe)_2Si$ phases, while in the alloy B(Si) with the excess of Si there was a mixture of cubic α-$Al_{12}(Mn,Fe)_2Si$ and hexagonal α-$Al_{15}(Mn,Fe)_3Si_2$ phases. This observation corresponds with the results of Westerman [20], Cama [21], Cieslar et al. [22] and Slámová et al. [23].

Some of the $Al_6(Mn,Fe)$ phase transformed to the cubic alpha phase (6-to-α transformation [24,25]) during the second step of the precipitation annealing at 450 °C at 5.2 mm thickness. But the transformation was not complete and the phase difference between the alloys persisted. The constiuent phase difference and higher silicon content in the solid solution of alloy B(Si) were at the origin of the differentiation of the microstructure and properties of the alloys during further downstream processing.

The plots in Fig. 3a and d show that the density of small particles after cold rolling from 5.2 to 0.3 mm and annealing 550 °C/3 h in the alloy A(Fe) was substantially reduced, while in the alloy B(Si) it remained almost constant. Nevertheless, the density of coarser particles (>400 nm) increased in both alloys, indicating coarsening of the precipitates (Fig. 3b and e). So there were several simultaneous processes acting at the same time: (i) nucleation of new dispersoids (observed up to the temperature of 500 °C [26]), (ii) 6-to-α transformation and coarsening of dispersoids, and (iii) partial particle dissolution and re-enrichment of the solid solution in Mn and Si [22]. In the case of alloy B(Si) there was a sufficient amount of silicon in the solid solution. In consequence, the dissolution and nucleation rate became equal and so the density of small particles after intermediate annealing 550 °C/3 h remained almost unchanged, while the density of coarse particles increased. On the other hand, in the case of alloy A(Fe) the particle size evolution was controlled by further coarsening of coarse particles on the expense of dissolution of the small ones. As the alloys contained also Zr addition, the dragging effect of Mn-rich dispersoids was assisted by fine Al_3Zr particles. Although these particles give a brighter contrast in BSE signal due to the high atomic number of Zr, they were not treated separately. From FEG SEM micrographs it can be seen that they nucleated sometimes heterogeneously on the Mn-rich dispersoids, sometimes homogeneously in the matrix. It is known that their distribution in Al–Mn alloys is not uniform due to microsegregation of Zr during casting and its slow diffusion rate [6]. As the nucleation of Al_3Zr particles is easier at clusters of Si [4,15,27,28], the higher density of small particles in the alloy B(Si) could be also caused by an increased number of Al_3Zr precipitates due to a higher silicon concentration in the solid solution of this alloy.

The density of coarse particles (>1.5 μm) in the alloy A(Fe) substantially increased after each thermo-mechanical operation, while the distribution of corresponding particles in the alloy B(Si) did not change significantly during the whole downstream processing (Fig. 3c and f). The alloy A(Fe) thus more easily recrystallized due to particle stimulated nucleation mechanism (Fig. 2a). Its susceptibility to recrystallization was furthermore supported by a low density of small particles 30–160 nm, which reduced after precipitation annealing at 5.2 mm thickness with each heat treatment in an important manner (Fig. 3a). On the other hand, the density of fine particles in the alloy B(Si) was much higher, it remained almost constant down to the intermediate thickness of 0.3 mm and reduced to a smaller extent at the final gauge (Fig. 3d), thus exerting an effective dragging force on subgrain and grain boundaries. In consequence, the recrystallization resistance of the alloy B(Si) at the final gauge was much higher (Fig. 5).

5. Conclusions

The influence of Si and Fe on the secondary phase particle distribution and recrystallization response of two industrially twin-roll cast Al–Mn alloys with Zr addition was studied. The main results can be summarized as follows:

(1) The constituent phases in the alloy A(Fe) with higher content of iron were $Al_6(Fe,Mn)$ and cubic α-$Al_{12}(Mn,Fe)_3Si$, while in the alloy B(Si) with higher content of silicon a mixture of cubic α-$Al_{12}(Mn,Fe)_3Si$ and hexagonal α-$Al_{15}(Mn,Fe)_3Si_2$ phases were found. Both alloys contained also very coarse blocks or needles of primary Al_3Zr phase.
(2) The density of coarse particles (>1.5 μm) in the alloy A(Fe) steadily increased during downstream processing. At the same time, the density of small precipitates (30–160 nm) reduced in an important manner, and so this alloy recrystallized easily due to particle stimulated mechanism.
(3) The alloy B(Si) with higher content of silicon showed much higher recrystallization resistance, because the distribution of coarse particles did not change significantly during whole downstream processing. Simultaneously, a high density of fine particles produced by precipitation annealing remained almost constant down to the intermediate thickness of 0.3 mm and reduced to a smaller extent at the final gauge.

Acknowledgements

This research has been supported by the Czech Technical University in Prague in the frame of the project SGS 10/301/OHK4/3T/14.

References

[1] A. Kawahara, A. Niikura, T. Doko, Furukawa Rev. 24 (2003) 81–87.
[2] F.J. Humphreys, M. Hatherly, Recrystallization and related annealing phenomena, 2nd ed., Elsevier, Amsterdam, 2004.
[3] A. Røyset, N. Ryum, Int. Mater. Rev. 50 (2005) 19–44.
[4] H. Westengen, O. Reiso, L. Auran, Aluminium 12 (1980) 768–775.
[5] J.D. Robson, P.B. Prangnell, Acta Mater. 49 (2001) 599–613.
[6] Z. Jia, G. Hua, B. Forbord, J.K. Solberg, Mater. Sci. Eng. A 444 (2007) 284–290.
[7] O. Izumi, D. Oelschlägel, Scripta Metall. 3 (1969) 619–622.
[8] E. Nes, Acta Metall. 20 (1972) 499–506.
[9] M.S. Zedalis, M.E. Fine, Metall. Trans. A 17 (1986) 2187–2198.
[10] R.B.C. Cayless, ASM Handbook, Vol. 2, Properties and Selection: Nonferrous Alloys and Special Purpose Materials, ASM International, Materials Park, OH, 1990, pp. 15–61.
[11] P. Kolby, C. Sigli, in: T.H. Sanders, E.A. Starke (Eds.), Proc. ICAA4, Atlanta, USA, Georgia Institute of Technology, 1994, pp. 508–511.
[12] P.C.M. de Haan, J. van Rijkom, J.A.H. Søntgerath, Proc. ICAA5, Grenoble, France, Mater. Sci. Forum 217–222, 1996, pp. 765–770.
[13] J.D. Robson, Mater. Sci. Eng. A 338 (2002) 219–229.
[14] Y.J. Li, L. Arnberg, Acta Mater. 51 (2003) 3415–3428.
[15] F. Nakamura, S. Hirosawa, T. Sato, in: J.F. Nie, A.J. Morton, B.C. Muddle (Eds.), Proc. ICAA9, Brisbane, Australia, Institute of Materials Engineering Australia Ltd., North Melbourne, 2004, pp. 582–587.
[16] Z. Jia, G. Hua, B. Forbord, J.K. Solberg, Mater. Sci. Eng. A 483–484 (2008) 195–198.
[17] M. Karlík, M. Slámová, T. Mánik, Kovove Mater. 47 (2009) 139–146.
[18] E. Anselmino, A. Miroux, S. van der Zwaag, Mater. Charact. 52 (2004) 289–300.
[19] J. Ondráček, Quantitative analysis of fine particles in Al–Mn alloys, BSc. Thesis, Czech Technical University in Prague, Faculty of Nuclear Sciences and Physical Engineering, 2009, 46 p. (in Czech).
[20] E.J. Westerman, in: J.G. Morris, H.D. Merchant, E.J. Westerman, P.L. Morris (Eds.), Aluminium Alloys for Packaging, TMS Warrendale, PA, 1993, pp. 1–16.
[21] H. Cama, J. Worth, P.V. Evans, A. Bosland, J.M. Brown, in: J. Beech, H. Jones (Eds.), SP'97 Proceedings of the 4th Decennial International Conference on Solidification Processing, Univeristy of Sheffield, Sheffield, 1997, pp. 555–558.
[22] M. Cieslar, M. Slámová, J. Uhlíř, C. Coupeau, J. Bonneville, Kovove Mater. 45 (2007) 91–98.
[23] M. Slámová, P. Sláma, M. Cieslar, in: W.J. Poole, M.A. Wells, D.J. Lloyd (Eds.), Proc. ICAA-10, Vancouver, Canada, Mater. Sci. Forum 519–521, 2006, pp. 365–370.
[24] D.T.L. Alexander, A.L. Greer, Acta Mater. 50 (2002) 2571–2583.
[25] Y.J. Li, L. Arnberg, Mater. Sci. Eng. A 347 (2003) 130–135.
[26] Y.J. Li, L. Arnberg, Proc. ICAA8, Cambridge, UK, Mater. Sci. Forum 396–402, 2002, pp. 875–880.
[27] T. Sato, A. Kamio, W. Lorimer, Proc. ICAA5, Grenoble, France, Mater. Sci. Forum 217–222, 1996, pp. 895–900.
[28] N.A. Belov, A.N. Alabin, V.V. Istomin-Kastrovskiy, in: J.F. Nie, A.J. Morton, B.C. Muddle (Eds.), Proc. ICAA9, Brisbane, Australia, Institute of Materials Engineering Australasia Ltd., North Melbourne, 2004, pp. 1270–1275.